FULL PAPER

Cancer Therapy

ADVANCED
FUNCTIONAL
MATERIALS
www.afm-journal.de

Traceable Nanoparticles with Spatiotemporally Controlled Release Ability for Synergistic Glioblastoma Multiforme Treatment

Zhiguo Lu, Yan Li, Yuanjie Shi, Yanhui Li, Zuobing Xiao, and Xin Zhang*

Doxorubicin (DOX), one of the most widely used clinical antineoplastics, has ineffective therapeutic efficacy on glioblastoma multiforme (GBM) with extremely short survival time due to many obstacles such as blood–brain barrier (BBB), tumor angiogenesis, and glioblastoma stem cells (GSCs). To overcome, biocompatible nanoparticles named CARD-B6 loading three clinical drugs are developed. Unlike other nanomedicines, CARD-B6, with the ability of spatiotemporally controlled release, maximize the effectiveness of DOX. (1) After CARD-B6 cross the BBB via B6, combretastatin A4 that is first released via protonation of poly (β-amino ester) specifically destroys angiogenesis to facilitate the interaction between GBM and CARD-B6. (2) Internalized into glioblastoma cells later, DOX is released via the breakage of amido bond to induce apoptosis, which is facilitated by the simultaneously released all-trans retinoic acid (ATRA). (3) After endocytosis into GSCs, the rapidly released ATRA induces the GSCs differentiation and downregulates the survival pathways, which enhances the sensitivity of GSCs to the subsequently released DOX. This synergistic antitumor effect significantly extends survival time of GBM mouse model. CARD-B6 are traced by superparamagnetic iron oxide nanocubes with high r_2 relaxivity for magnetic resonance imaging. Therefore, the traceable CARD-B6 with spatiotemporally controlled release ability are emerging as a powerful platform for GBM treatment.

1. Introduction

Doxorubicin (DOX) is one of the most widely used clinical antineoplastic drugs.[1] However, it has ineffective therapeutic efficacy on glioblastoma multiforme (GBM) due to many obstacles such as blood–brain barrier (BBB), tumor angiogenesis, and glioblastoma stem cells (GSCs).[2] First, the BBB restricts the passage of drugs into the brain and shields the tumor tissues from exposure to DOX.[3] Second, angiogenesis presents another hindrance for DOX reaching the tumor cells and satisfies the voracious nutrients demands of the tumor growth.[4] Third, the effect of DOX on GBM is impaired by the intrinsic chemoresistance of GSCs.[5] Hence, it is crucial to overcome these obstacles to enhance the therapeutic efficacy of DOX for GBM.

Several efforts have been made to solve these abovementioned problems. Park et al. utilized focused ultrasound combined with microbubbles to disrupt the BBB, which enhanced the delivery of DOX to the tumor site.[6] Nevertheless, this aggressive approach would leave the patients in danger without the protection of BBB. Sophorolipid–gellan gum–gold nanoparticles (NPs) were constructed by Dhar et al. to enhance the cytotoxicity of DOX toward GSCs by promoting the cellular uptake, but this method did not conquer the chemoresistance of the GSCs.[7] In particular, neither of these methods could surmount the problems associated with the BBB, tumor angiogenesis, and chemoresistance of the GSCs simultaneously.

In this study, a DOX-based combination chemotherapy was employed to overcome these obstacles synergistically. Combretastatin A4 (CA4), a widely used clinical antiangiogenic drug, has been proved to overcome the barrier of angiogenesis.[8] All-trans retinoic acid (ATRA), a widely used aromatic drug, was employed to induce the GSCs differentiation into glioblastoma cells, which could conquer their chemoresistance.[9] In particular, according to previous studies, ATRA could also enhance the chemotherapy-induced apoptosis of glioblastoma cells via downregulation of telomerase activity and the survival pathways.[10] Unfortunately, the intrinsic deficiencies of these drugs, such as short plasma half-life and poor ability of crossing the BBB, limited their application. Meanwhile, it is expected that these three drugs should be packaged together and be delivered to the tumor region rather than be delivered individually after intravenous administration. Then the package of three drugs should be controllably released into their corresponding active sites. Therefore, it is necessary to develop a highly efficient and safe codelivery system with the ability of spatiotemporally controlled release.

Z. Lu, Dr. Y. Li, Y. Shi, Y. Li, Prof. X. Zhang
State Key Laboratory of Biochemical Engineering
Institute of Process Engineering
Chinese Academy of Sciences
Beijing 100190, P. R. China
E-mail: xzhang@ipe.ac.cn

Z. Lu
School of Chemistry and Chemical Engineering
University of Chinese Academy of Sciences
Beijing 100049, P. R. China

Prof. Z. Xiao
School of Perfume and Aroma Technology
Shanghai Institute of Technology
Shanghai 201418, P. R. China

Prof. Z. Xiao
Shanghai Research Institute of Fragrance and Flavor Industry
Shanghai 200232, P. R. China

**ADVANCED
SCIENCE NEWS**

www.advancedsciencenews.com

**ADVANCED
FUNCTIONAL
MATERIALS**

www.afm-journal.de

To satisfy these conditions, functional materials including a peptide motif B6, 1,2-dioleoylsn-glycero-3-phosphoethanolamine-n-[poly (ethylene glycol)] 2000 (DSPE-PEG$_{2000}$), poly (β-amino ester) (PAE), and azobenzene (AZO) were used in the codelivery system. B6, a representative peptide with high affinity for transferrin receptors, has shown potential for enabling the NPs to reach the brain.[11] The biocompatible DSPE-PEG$_{2000}$ could extend the circulation time of the codelivery system.[12] The acid-sensitive PAE was used to control the release of CA4 in the GBM microenvironment and to accelerate the endosomal/lysosomal escape of the codelivery system in the glioblastoma cells and GSCs.[13] Additionally, the tissue oxygen partial pressure is substantially lower for the GSCs than for the glioblastoma cells.[14] In our previous study, the AZO bond could break within 5 minutes under hypoxic condition, which was much faster than the breakage of the amido bond.[15] Therefore, the AZO bond and the amido bond were used to control the release of ATRA and DOX in the GSCs sequentially. Rapidly released ATRA could induce the GSCs differentiation and downregulate the survival pathways, which could enhance the sensitivity of the GSCs to the subsequently released DOX. Moreover, superparamagnetic iron oxide nanocubes (SPIONs) with high r$_2$ relaxivity for magnetic resonance imaging (MRI) were introduced to trace the accumulation of the codelivery system in the tumor tissue.[16] As shown in **Scheme 1**A, B6 was linked with amphiphilic DSPE-PEG$_{2000}$. ATRA and DOX were conjugated with PAE via amido-AZO (-A-AZO-) and amido bond (-A-) to form two inert hydrophobic macromolecular prodrugs PAE-A-AZO-ATRA and PAE-A-DOX, respectively. The traceable NPs were self-assembled via the hydrophobic interaction between DSPE and the agents, in which the hydrophobic CA4, PAE-A-AZO-ATRA, PAE-A-DOX and SPIONs were loaded in the core of NPs. Therefore, the traceable NPs with B6 loading three drugs $^{(CA4+AZO-ATRA+DOX+SPIONs)}$NPs-B6 (CARD-B6) were constructed for GBM therapy.

CARD-B6 with the ability of spatiotemporally controlled release can deliver these agents to their corresponding target sites. As presented in Scheme 1B, (1) CARD-B6 were expected to accumulate in the GBM microenvironment after across the BBB by receptor-mediated endocytosis.[17] (2) CARD-B6 could be swelled to first release small molecular CA4 via the protonation of PAE at pH 6.5 in a GBM microenvironment.[18] The released CA4 specifically destroyed the angiogenesis to cut off the essential nutrition supply for GBM growth and facilitated the interaction between the glioblastoma mass and the DOX-loaded NPs. (3) After being internalized into the glioblastoma cells, it was hypothesized that PAE-A-AZO-ATRA, PAE-A-DOX, and SPIONs could escape from the endosomes/lysosomes by proton sponge effect of PAE at pH 5.0. ATRA and DOX were then released into the nuclei simultaneously via the breakage of the amido bond.[19] ATRA enhanced the cytotoxicity of DOX on the glioblastoma cells by downregulation of telomerase activity and survival-associated pathways. (4) After endocytosis into the GSCs, ATRA was rapidly released into the nuclei due to the stimulate-response breakage of the AZO bond under hypoxic condition. ATRA induced the GSCs differentiation into glioblastoma cells and then enhanced the sensitivity of differentiated glioblastoma cells to the subsequently released DOX.

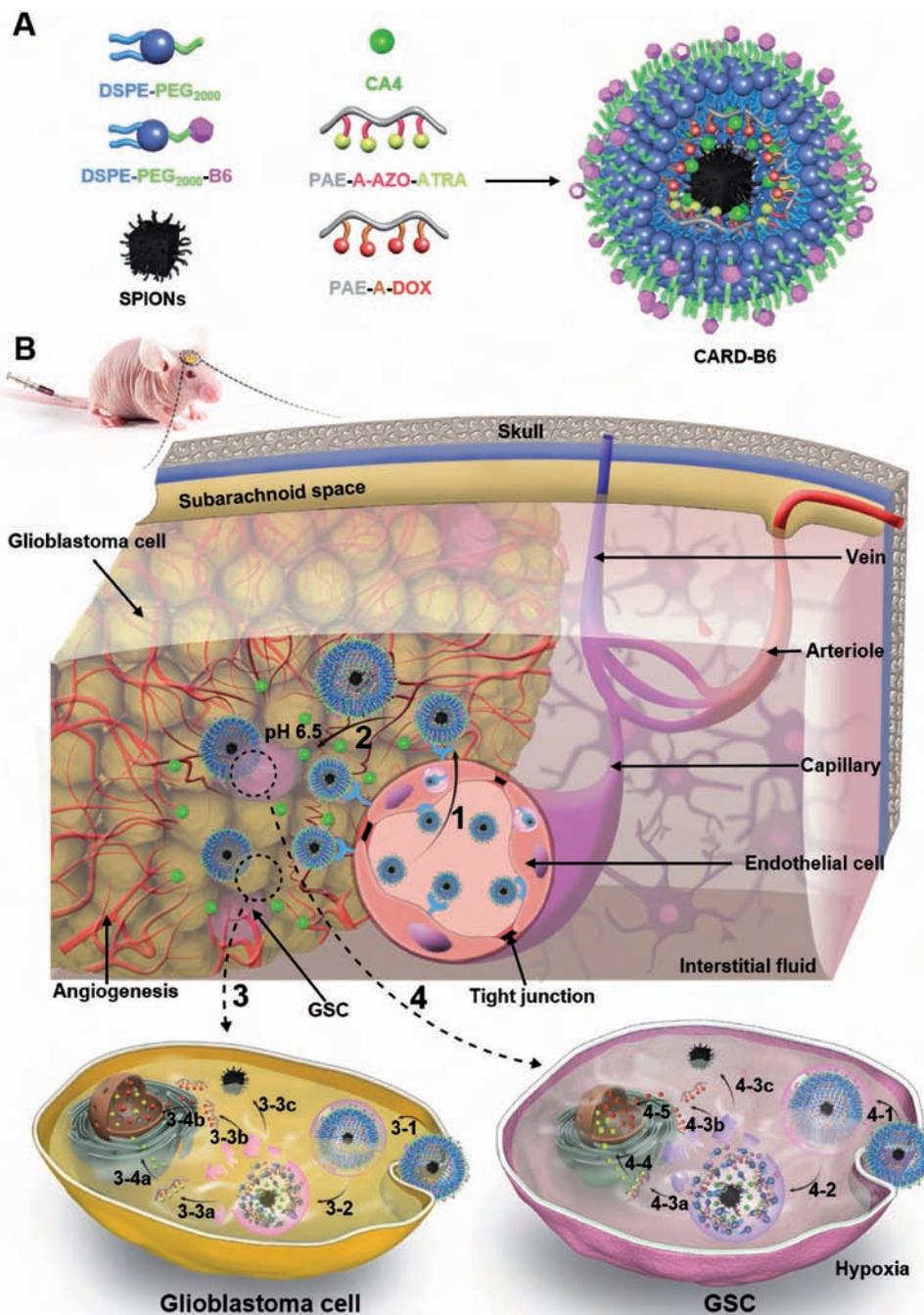During this process, CARD-B6 were traced by the SPIONs with a high r$_2$ relaxivity for MRI.

2. Results and Discussion

2.1. Preparation and Characterization of CARD-B6

DSPE-PEG$_{2000}$-Mal was chemically modified with B6 via an addition reaction (Figure S1, Supporting Information).[20] The chemical composition of the obtained lipid was studied by matrix-assisted laser desorption ionization time-of-flight mass spectrometry. The peak of the DSPE-PEG$_{2000}$ shifted to around 3888 m/z, which confirmed the successful synthesis of DSPE-PEG$_{2000}$-B6 (Figure S2, Supporting Information). ATRA was linked to PAE via an amido-AZO bond. The ^{1}H NMR spectra in Figure S3 (Supporting Information) confirmed that the hypoxia responsive linker AZO was successfully linked to ATRA. PAE was synthesized by a Michael addition reaction.[21] The results of the ^{1}H NMR spectra and gel permeation chromatography (Figures S3 and S4, Supporting Information) showed that PAE with a molecular mass of 3500 was successfully synthesized. The protonation of PAE was determined by acid–base titration. PAE showed good buffering capacity around pH 6.5 (Figure S5, Supporting Information), which was the extracellular pH of the GBM microenvironment. Confirmation that drugs were conjugated with PAE was obtained by ^{1}H NMR (Figure S6, Supporting Information). The peaks of DOX and ATRA were detected in DMSO-d_6, which indicated the successful synthesis of the inert macromolecular prodrugs PAE-A-AZO-ATRA and PAE-A-DOX. As a control, nonhypoxia responsive PAE-amido-benzidine-ATRA (PAE-A-BZD-ATRA) was also successfully obtained. The drug loading efficiency of DOX for the PAE-A-DOX polymer was 58.37% as calculated by fluorospectrophotometry analysis. The values were 14.53% and 16.23% of ATRA for the PAE-A-AZO-ATRA and PAE-A-BZD-ATRA polymers as calculated by UV–vis spectrophotometer, respectively (Figure S7, Supporting Information).

The hydrophobic SPIONs were synthesized via high-temperature thermal decomposition. The morphology and size of SPIONs were measured by transmission electron microscope (TEM). As shown in Figure S8 (Supporting Information), the SPIONs were cubic in shape with a diameter of about 20 nm. Cubic SPIONs were chosen in our system because they possessed high r_2 relaxivity for highly sensitive in vivo MRI of brain tumor.

Next, CARD-B6 were constructed for GBM therapy. As displayed in Table S1 (Supporting Information), NPs without B6 $^{(CA4+AZO-ATRA+DOX+SPIONs)}$NPs (CARD), nonhypoxia responsive $^{(CA4+BZD-ATRA+DOX+SPIONs)}$NPs-B6 (CBRD-B6), traceable NPs without ATRA (CD-B6), without DOX (CAR-B6), without CA4 (ARD-B6), and empty traceable NPs (Empty NPs) were prepared for comprehensive study. The assembly of the traceable NPs in phosphate buffered saline (PBS, pH = 7.4) was investigated by dynamic light scattering and TEM. As shown in **Figure 1**A, the average diameters of all NPs were within 100 nm with zeta potential ranging from −0.50 to −0.90 mV (Figure S9, Supporting Information). The TEM image showed that CARD-B6 presented monodispersed structure (Figure 1B). Additionally,

Scheme 1. A) The structural composition and preparation of CARD-B6. CARD-B6 were self-assembled via the hydrophobic interaction. B) The schematic diagram of drug delivery. (1) CARD-B6 accumulated in GBM microenvironment after across BBB. (2) CA4 was first released in tumor microenvironment at pH 6.5. (3-1) The remaining NPs were internalized into glioblastoma cells via endocytosis. (3-2) The NPs were further swelled and burst in the endosomes/lysosomes at pH 5.0. PAE-A-AZO-ATRA (3-3a), PAE-A-DOX (3-3b), and SPIONs (3-3c) were released into cytoplasm. ATRA (3-4a) and DOX (3-4b) were then released simultaneously into nuclei due to the breakage of amido bond and induced apoptosis of the glioblastoma cells synergistically. (4-1) The remaining NPs were also internalized into GSCs via endocytosis. (4-2) The NPs were further swelled and burst when encountering the endosomal/lysosomal environment with pH 5.0. PAE-A-AZO-ATRA (4-3a), PAE-A-DOX (4-3b), and SPIONs (4-3c) were then released into cytoplasm. (4-4) ATRA was rapidly released due to the breakage of AZO bond in hypoxic condition and entered the nuclei to induce the GSCs to differentiate into glioblastoma cells. DOX was released later due to the breakage of amido bond and entered the nuclei to induce the apoptosis of the differentiated glioblastoma cells synergistically with ATRA.

the encapsulation had almost no influence on the morphology of the SPIONs. As displayed in Figure 1C, CARD-B6 exhibited good serum stability in 10% fetal bovine serum due to the

modification of PEG, which was beneficial for long circulation in vivo. Moreover, the influence of the PAE protonation on the CARD-B6 was studied by dynamic light scattering. As shown
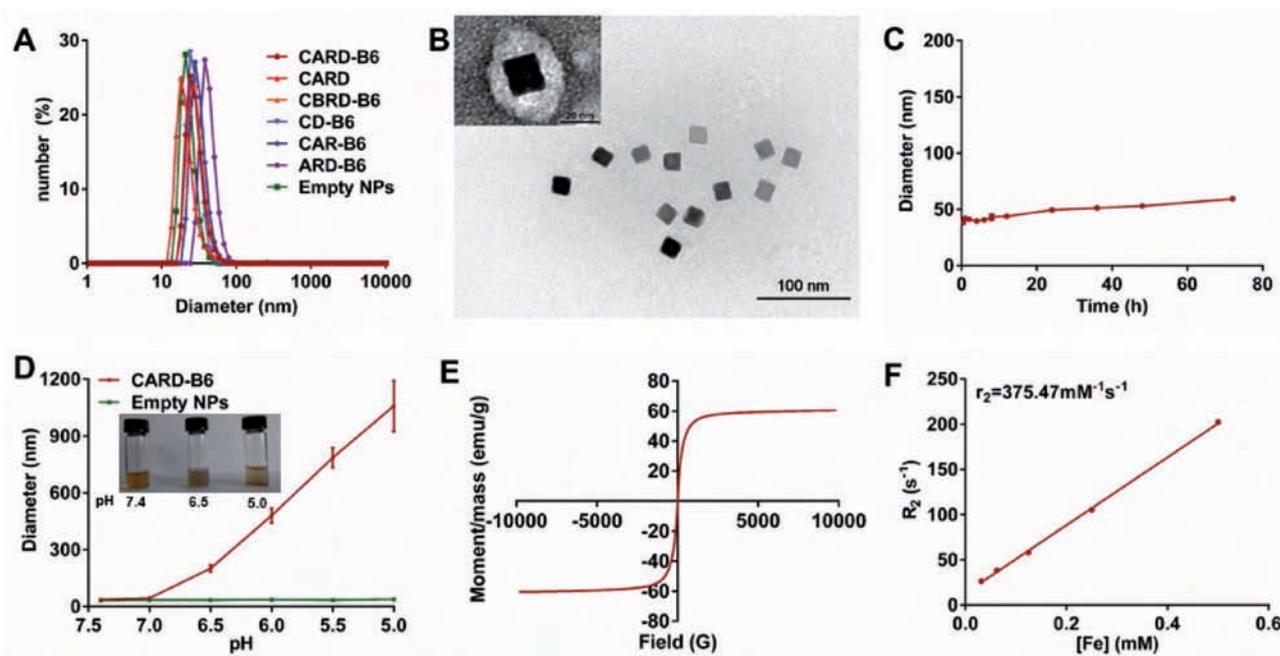
**ADVANCED
SCIENCE NEWS**
www.advancedsciencenews.com

**ADVANCED
FUNCTIONAL
MATERIALS**
www.afm-journal.de

Figure 1. The characterization of NPs. A) The size distribution of NPs. B) The TEM image of CARD-B6. The scale bar: 100 nm. The image magnified was the TEM image with negative staining. The scale bar: 20 nm. C) The serum stability of CARD-B6. D) The diameters of NPs at different pH values. Insert picture showed CARD-B6 in buffer solution with different pH values. E) The magnetization curve of CARD-B6. F) A plot of R_2 as a function of the Fe concentration of CARD-B6. The mean $\pm$ SD is shown ($n = 3$).

in Figure 1D, the NPs with PAE exhibited pH-dependent diameters. The diameter of CARD-B6 increased from 37.84 nm at pH 7.4 to 201.35 nm at pH 6.5. In comparison, there was no significant change in the diameters of the NPs without PAE over the pH range studied. These results indicated that CARD-B6 could be swelled due to the protonation of PAE, which was beneficial for the controlled release of CA4 in the acidic GBM microenvironment. Furthermore, the diameter of CARD-B6 increased to 1059.26 nm as the pH value dropped to 5.0. In addition, when the pH value dropped from 7.4 to 6.5, the solution started to be cloudy. When the pH value dropped to 5.0, there was precipitation in the solution. These results indicated that CARD-B6 could be demicellization in the acidic endosomes/lysosomes to release PAE-A-AZO-ATRA, PAE-A-DOX, and SPIONs.

High-quality synthetic iron oxide NPs as MR contrast were typically prepared through the thermal decomposition of metal–complex precursors in hot nonhydrolytic organic solution containing surfactants. However, the SPIONs with hydrophobic ligand presented a low MR relaxivity due to limited access of water protons. Therefore, it is necessary to design the hydrophilic ligand shell to attain high MR relaxivity. As shown in Figure S10 (Supporting Information), surface hydrophilic modification significantly enhances their dispersity in water for CARD-B6. To assess the magnetic properties of the traceable NPs for MRI application, the magnetization curve and the r_2 value were measured. The magnetization curve exhibited no remnant magnetization and coercivity. The saturation magnetization was about 60 emu g^{-1} (Figure 1E). Furthermore, the r_2 value was calculated by measuring the change in the spin–spin relaxation rate (R_2) per unit iron concentration. As shown in Figure 1F, the r_2 value of the CARD-B6 was 375.47 mM^{-1} s^{-1},

which was high enough for in vivo MRI application of GBM therapy.

2.2. In Vitro Drug Release Behavior of NPs

The encapsulation efficiency of CA4, ATRA, and DOX was 75.3%, 77.8%, and 78.4%, respectively. It was expected that CA4, PAE-A-AZO-ATRA, and PAE-A-DOX should be simultaneously delivered to the tumor region and controllably released into their active sites sequentially after systemic administration. If drugs were encapsulated in separate NPs, it was hard to guarantee them. This uncontrollable delivery and release may reduce the therapeutic effect remarkably. Therefore, CA4, PAE-A-AZO-ATRA, and PAE-A-DOX should be encapsulated in the same NPs. To detect the drugs in NPs via fluorometry, a hydrophobic fluorescent molecule Cy5 with similar characteristics as CA4 was used to replace the drug molecule CA4 because CA4 had no fluorescence. As shown in Figure S11 (Supporting Information), 3D-SIM images of CARD-B6 showed that the fluorescence of DOX was overlapped with that of Cy5 in NPs and the colocalization coefficient was 0.9895, which indicated that CA4 and PAE-A-DOX were in the same NPs. In addition, the images of U-87 MG cells after incubation with CARD-B6 were taken by CLSM. Three drugs encapsulated in separate NPs were used as controls. The fluorescences of ATRA, DOX, and Cy5 were colocalized in the U-87 MG cell to form white fluorescence after incubation with CARD-B6 (Figure S12A, Supporting Information). By contrast, the fluorescences of these three molecules were not completely colocalized after incubation with the separate NPs (Figure S12B, Supporting Information). The
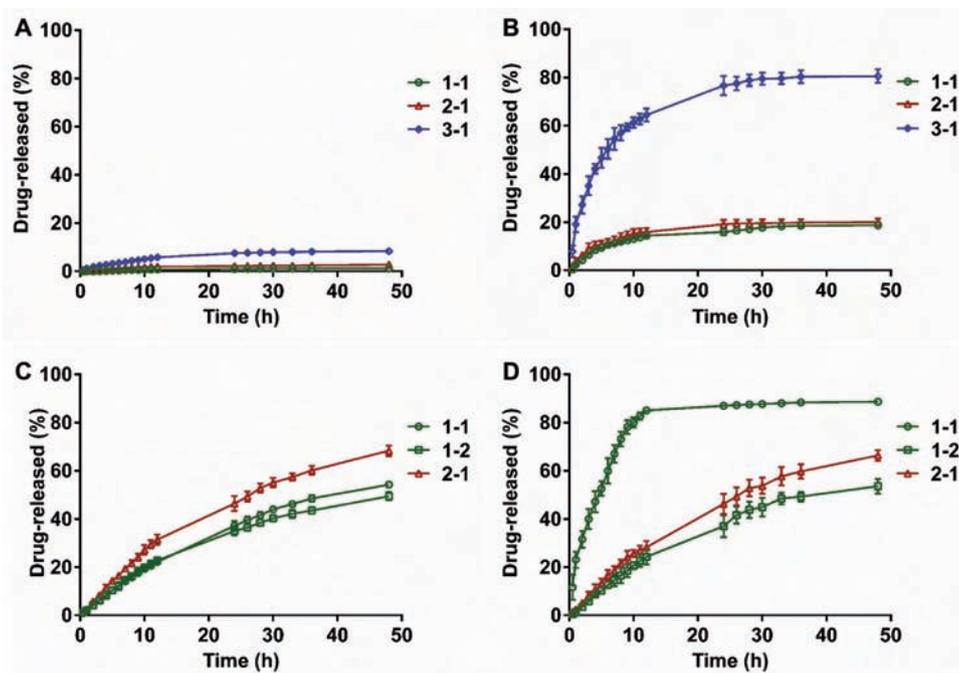
Figure 2. The cumulative release profiles of drugs in different conditions at 37 °C with A) pH = 7.4; B) pH = 6.5; C) pH = 5.0. D) Hypoxic condition at pH 5.0. Samples: (1-1) ATRA in CARD-B6; (2-1) DOX in CARD-B6; (3-1) CA4 in CARD-B6; (1-2) ATRA in nonhypoxia responsive CBRD-B6. The mean ± SD is shown ($n = 3$).

colocalization coefficients after incubation with CARD-B6 were higher than those with separate NPs (Figure S12C, Supporting Information). In summary, these results indicated that these three drug molecules were in the same NPs for CARD-B6.

CARD-B6 should be able to spatiotemporally controlled release of CA4, ATRA, and DOX to their active sites in an orderly manner. The release profiles of these three drugs were measured in different conditions. As shown in **Figure 2**A, the release profiles of all drugs were within 10% at pH 7.4 for 48 h incubation, suggesting that there was no obvious release of the drugs. Therefore, CARD-B6 were stable in physiological condition. The drug release behavior was then detected in a pH 6.5 solution, which imitated the GBM microenvironment (Figure 2B). The amount of CA4 released from CARD-B6 reached 64.47% at pH 6.5 after 12 h, whereas the proportions for ATRA and DOX were only 14.37% and 15.93%, respectively. The results demonstrated that CA4 could be released quickly in the GBM extracellular pH microenvironment due to the swell of the NPs induced by the protonation of PAE. The first-released CA4 was able to destroy the angiogenesis to expose the glioblastoma cells and the GSCs to the remaining NPs.

Subsequently, the release profiles of the drugs in the glioblastoma cells were measured. From the release graph in Figure 2C, the conjugated ATRA and DOX had continuous release profiles after incubation at pH 5.0, which simulated the endosomes/lysosomes of cells. The values were 54.24% and 68.37% for ATRA and DOX from CARD-B6 and 49.46% for ATRA from CBRD-B6 after 48 h of incubation, respectively. The results showed that ATRA and DOX were released at almost the same rate due to the breakage of the amido bond. Free ATRA could downregulate telomerase activity of glioblastoma cells and further enhance the effect of DOX.

Since liver microsome enzymes could cleave nitroimidazole derivatives under hypoxia, hypoxia responsive release profiles were detected after incubation with rat liver microsomes enzymes. The release of ATRA from CARD-B6 was stimulated by the hypoxia and reached 85.11% after 12 h incubation, which was much higher than the value for ATRA from the nonhypoxia responsive CBRD-B6 (24.28%) (Figure 2D). These results indicated that the use of AZO facilitated the rapid release of ATRA from CARD-B6 under hypoxic condition. In addition, the release profile of DOX from CARD-B6 under hypoxic condition showed a relatively continuous and slow process. It was 28.23% and 66.34% of DOX released from CARD-B6 after 12 and 48 h incubation under hypoxic condition, respectively. The rapidly released ATRA could induce the differentiation of GSCs in advance and inhibit their chemoresistance to the later-released DOX. To sum up, CARD-B6 with spatiotemporally controlled release ability could release CA4, ATRA, and DOX into their target sites in sequence to maximize the antitumor effect of DOX.

2.3. Transportation Across the In Vitro BBB Model

The BBB formed by brain microvessel endothelial cells is linked together by tight junctions, which restricts the transfer of the NPs from the bloodstream into the brain. Therefore, the BBB is a major challenge for GBM therapy. In our system, the NPs were modified with B6 to overcome this barrier. The permeability of B6 was quantitatively measured by a cell-based in vitro BBB model. In this two-chamber transwell system, bEND.3 and U-87 MG cells were grown on the bottom of upper and lower chambers, respectively (**Figure 3**A). The integrity

**ADVANCED
SCIENCE NEWS**
www.advancedsciencenews.com

**ADVANCED
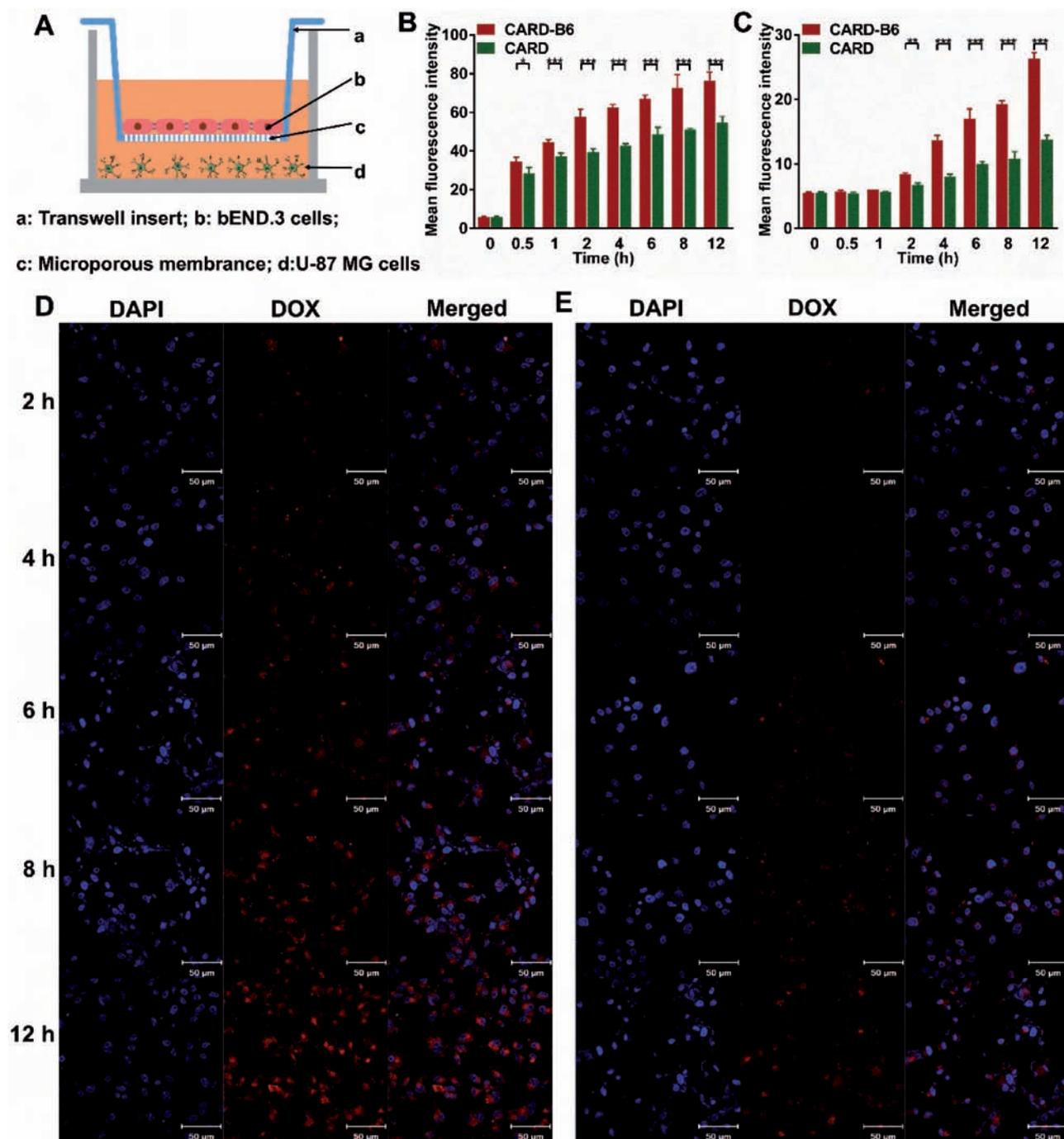FUNCTIONAL
MATERIALS**
www.afm-journal.de

Figure 3. Transport of DOX-loaded NPs across the in vitro BBB model. A) The structure of transwell chambers. U-87 MG and bEND.3 cells were cocultured in transwell chambers imitating BBB. The cellular uptake of different NPs in B) bEND.3 and C) U-87 MG cells was detected via flow cytometry. The cellular uptake of D) CARD-B6 and E) CARD in U-87 MG cells was observed by CLSM. Nuclei were stained with 4′6-diamidino-2-phenylindole dihydrochloride (DAPI). The scale bars: 50 µm. The mean ± SD is shown ($n = 3$). *$P < 0.05$, **$P < 0.01$, ***$P < 0.005$.

of bEND.3 monolayer in vitro was evaluated by transendothelial electrical resistance.[22] After the transendothelial electrical resistance value reached 200 Ω cm², CARD-B6 and CARD were added to the upper chamber, respectively. The cellular uptake of DOX was measured by flow cytometry and confocal laser scanning microscope (CLSM). As shown in Figure 3B, the mean fluorescence intensity of DOX for CARD-B6 in the bEND.3

cells increased remarkably with the increase in time and was significantly higher than that of CARD at each time point. It was 70.22 for CARD-B6 at 12 h but only 48.54 for CARD. The permeability of the NPs into the lower chamber was determined by measuring the cellular uptake in the U-87 MG cells. As shown in Figure 3C, the DOX-loaded NPs were internalized into the U-87 MG cells starting at 2 h after incubation,

ADVANCED
SCIENCE NEWS
www.advancedsciencenews.com

ADVANCED
FUNCTIONAL
MATERIALS
www.afm-journal.de

suggesting that the NPs took 2 h to cross the bEND.3 layer. The mean fluorescence intensity was significantly higher for the NPs with the modification of B6 in the U-87 MG cells than for CARD without B6, which was attributed to their high permeability of B6 modification. These results were further verified via CLSM. The CLSM images (Figure 3D,E and Figure S13, Supporting Information) and quantitative results (Figure S14, Supporting Information) showed that the mean fluorescence intensity of DOX for CARD-B6 in the bEND.3 and U-87 MG cells was much higher than that for CARD at each time point. These results indicated that the B6 modification effectively conquered the barrier of BBB and promoted the permeation of the DOX-loaded NPs across the in vitro BBB model, which would enhance the accumulation of CARD-B6 in the GBM.

2.4. Cellular Uptake and Endosomal/Lysosomal Escape Analysis

The active sites of DOX in the glioblastoma cells and GSCs are nuclei. Therefore, the internalization and nuclei localization of DOX in the U-87 MG cells were investigated by CLSM. As shown in **Figure 4**A, free DOX was directly internalized into the nuclei and the fluorescence of DOX had no colocalization with the endosomes/lysosomes. The results were in agreement with our previous study that free drugs were internalized into cells via direct diffusion.[23] In comparison, a time-dependent

pattern in the cellular uptake of DOX was achieved by CARD-B6 (Figure 4B). The fluorescence of DOX was colocalized with LysoTracker Deep Red as yellow dots at 4 and 8 h, indicating that the NPs were internalized by the way of endocytosis. DOX was released via the breakage of the amido bond and entered the nuclei beginning at 12 h and was obviously accumulated in the nuclei after 24 h incubation, which was in agreement with the continuous release profile in Figure 2C. In addition, ATRA was tracked within the U-87 MG cells. As shown in Figure S15 (Supporting Information), a time-dependent pattern in the uptake of ATRA was achieved. After 4 h incubation, free ATRA entered the nuclei directly (Figure S15A, Supporting Information). By contrast, the ATRA from CARD-B6 started to enter the nuclei after 12 h incubation (Figure S15B, Supporting Information). Moreover, ultrathin sections of U-87 MG cells incubated with CARD-B6 were performed to track the SPIONs within the U-87MG cells. As shown in Figure S16 (Supporting Information), the accumulation of SPIONs in cells also demonstrated a time-dependent pattern for CARD-B6.

Subsequently, the distribution of DOX in the GSCs neurospheres was also observed via CLSM after incubation of CARD-B6 and free drugs (CA4 + ATRA + DOX). The mean fluorescence intensity of DOX also increased with the extension of time for the free drugs and CARD-B6 in GSCs (Figure 4C,D). It was 13.79 at 4 h and increased to 31.91 at 24 h for CARD-B6 at a depth of 40 µm (Figure S17a, Supporting
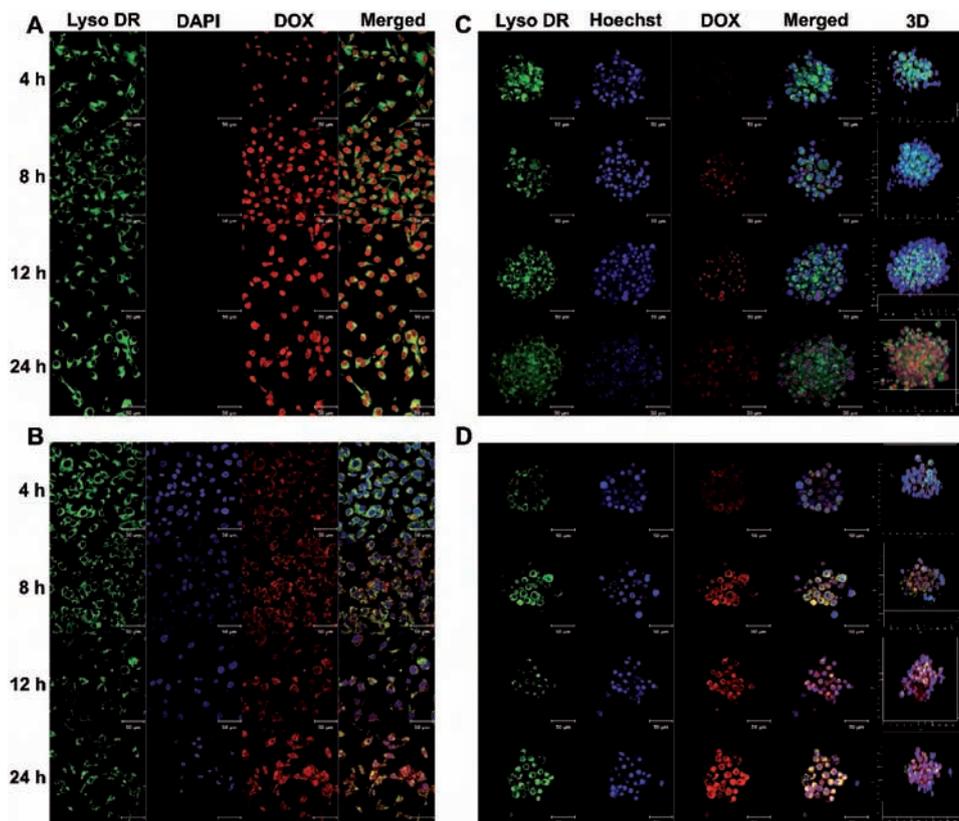

Figure 4. The distribution of free drugs and CARD-B6 in U-87 MG cells and GSCs spheres at 4, 8, 12, and 24 h, respectively. A) Free drugs in U-87 MG cells. B) CARD-B6 in U-87 MG cells. C) Free drugs in GSCs spheres. D) CARD-B6 in GSCs spheres. Endosomes/lysosomes were stained with LysoTracker Deep Red (Lyso DR) and nuclei were stained with DAPI and Hoechst 33342, respectively. The images were detected via CLSM. The scale bars: 50 µm.

ADVANCED
SCIENCE NEWS
www.advancedsciencenews.com

ADVANCED
FUNCTIONAL
MATERIALS
www.afm-journal.de

Information). Moreover, the mean fluorescence intensity of DOX for CARD-B6 at each depth was much stronger than that of free drugs at 24 h (Figure S17B, Supporting Information). These results demonstrated that the NPs facilitated the permeation of the hydrophobic DOX to the inner parts of the GSCs neurospheres. DOX started to continuously enter the nuclei of GSCs at 12 h. These results suggested that CARD-B6 were efficiently internalized into the glioblastoma cells and GSCs, and released the DOX into the nuclei for GBM therapy. In addition, ATRA was tracked within the GSCs under hypoxic condition. As shown in Figure S18 (Supporting Information), a time-dependent pattern in the uptake of ATRA was achieved. ATRA from free drugs entered the nuclei directly after 8 h incubation. ATRA from nonhypoxia responsive CBRD-B6 was endocytosed into GSCs after 4 h and started to enter the nuclei after 12 h. By contrast, ATRA from CARD-B6 was internalized into GSCs and started to enter the nuclei after 4 h. The results demonstrated that ATRA released from CARD-B6 was more rapid than that from nonhypoxia responsive CBRD-B6 in hypoxic environment. Additionally, the release of ATRA was faster than DOX from CARD-B6, which was beneficial for enhancing the effect of DOX on GSCs.

2.5. The Differentiation of GSCs In Vitro

The chemoresistance of the GSCs could protect them from DOX-induced apoptosis. Therefore, ATRA was introduced to overcome the chemoresistance via an induced differentiation of the GSC in advance. To evaluate the effect, the NPs and free ATRA were incubated with the GSCs under hypoxic condition. To avoid the cytotoxicity of DOX, hypoxia and nonhypoxia responsive NPs with only ATRA (AR-B6 and BR-B6) were used to measure the differentiation effect. The stemness of the GSCs was identified via the CD133 antibody, which is a specific marker for GSCs.[24] As shown in Figure S19 (Supporting Information), the cell spheres obtained via a serum-free suspending culture were CD133 positive. After coculture with empty NPs for 24 h, almost no GSC differentiation was observed (**Figure 5**A). After incubation with AR-B6 for 24 h, the percentage of $CD133^+$ cells decreased to 37.15% owing to the rapid release of ATRA in the hypoxic environment, which was comparable with the results for the free ATRA (32.69%). In comparison, $CD133^+$ cells decreased to 53.93% for the nonhypoxia responsive BR-B6. The results of 48 h showed the same trend that AR-B6 induced a greater amount of GSCs differentiation than BR-B6. This was mainly attributed to the rapid release of ATRA from the NPs with the AZO linker compared with the nonhypoxia responsive NPs. These results indicated that the faster breakage of the AZO bond under hypoxic condition accelerated the differentiation rate of the GSCs to overcome the barrier of chemoresistance in GBM therapy.

2.6. In Vitro Cytotoxicity

Tumor angiogenesis is another obstacle for GBM therapy of DOX. To investigate the antivascular effect of CARD-B6 and the cytotoxicity of DOX on glioblastoma cells and GSCs, two

groups of noncontact coculture models were applied to mimic the protection of angiogenesis in vitro (Figure 5B). The in vitro antitumor activity of the NPs was determined by (3-(4,5-dimethylthiazol-2-yl)-2,5-diphenyltetrazolium bromide (MTT) assay. Particularly, NPs were incubated in a solution with a pH value of 6.5 for 4 h to mimic the GBM extracellular pH. The pH value was adjusted to 7.4 prior to incubation with the cells. In all experiments, the empty NPs without drugs showed negligible cytotoxicity, indicating their excellent biocompatibility. The cell viability was decreased with increasing time and the cell viability for all cells was higher after 24 h than after 48 h. In the U-87 MG system, the NPs with CA4 induced significant apoptosis of the human umbilical vein endothelial cells (HUVECs) with a cell viability of approximately 13.40% after 24 h incubation, which was much lower than the value for ARD-B6 without CA4 50.32% (Figure 5C). The results indicated that the first-released CA4 promoted by the protonation of PAE could destroy the blood vessels, which exposed the U-87 MG cells to the remaining NPs. After endocytosis into the U-87 MG cells, the cell viability was only 7.53% for the NPs with DOX and ATRA, which was much lower than that for CD-B6 without ATRA (18.11%) and ARD-B6 without CA4 (20.05%) (Figure 5D). These results indicated that the destructive effect of CA4 on the HUVECs and the downregulation of survival pathways of ATRA could enhance the cytotoxicity of DOX on U-87 MG cells.

In the GSCs system, the cell viability of the HUVECs showed the same trend that NPs with CA4 decreased their viability to 6.78% at 48 h (Figure 5E). The cell viability of the GSCs was very different from that of U-87 MG. It decreased to approximately 13.04% for the CARD-B6, which was significantly lower than for other groups, especially the free drugs (CA4 + ATRA + DOX) at 48 h (Figure 5F). This confirmed that CA4 and ATRA had the expected effects on angiogenesis and GSCs, respectively. Specifically, the excellent anti-GSC effect of CARD-B6 was attributed to their controlled release ability that ATRA could be released quickly to induce the differentiation of the GSCs in advance and DOX was released in a sustained manner to kill the differentiated cells. These results indicated that CARD-B6 could destroy the tumor vascular and induce the differentiation of the GSCs simultaneously via controlled release of CA4, ATRA, and DOX to their corresponding active sites, which increased the toxicity of DOX on tumor cells.

2.7. Pharmacokinetics and Accumulation of the Traceable NPs in the Tumor Region

In order to evaluate the potential antitumor activity, the pharmacokinetics of the NPs were investigated. As shown in **Figure 6**A,B, the concentrations of CA4 and DOX were much higher for CARD-B6 than for free drugs (CA4 + ATRA + DOX) at all time points. It was 2.58 µg mL^{-1} of CA4 and 14.35 µg mL^{-1} of DOX for CARD-B6 5 min after the injection but only 0.63 µg mL^{-1} of CA4 and 3.29 µg mL^{-1} of DOX for the free drugs. The plasma concentrations of DOX and CA4 decreased rapidly in the free drugs group and hardly any drugs were detected 24 h after the injection. By contrast, there were still 0.32 µg mL^{-1} of CA4 and 1.37 µg mL^{-1} of DOX remaining

**ADVANCED
SCIENCE NEWS**
www.advancedsciencenews.com

**ADVANCED
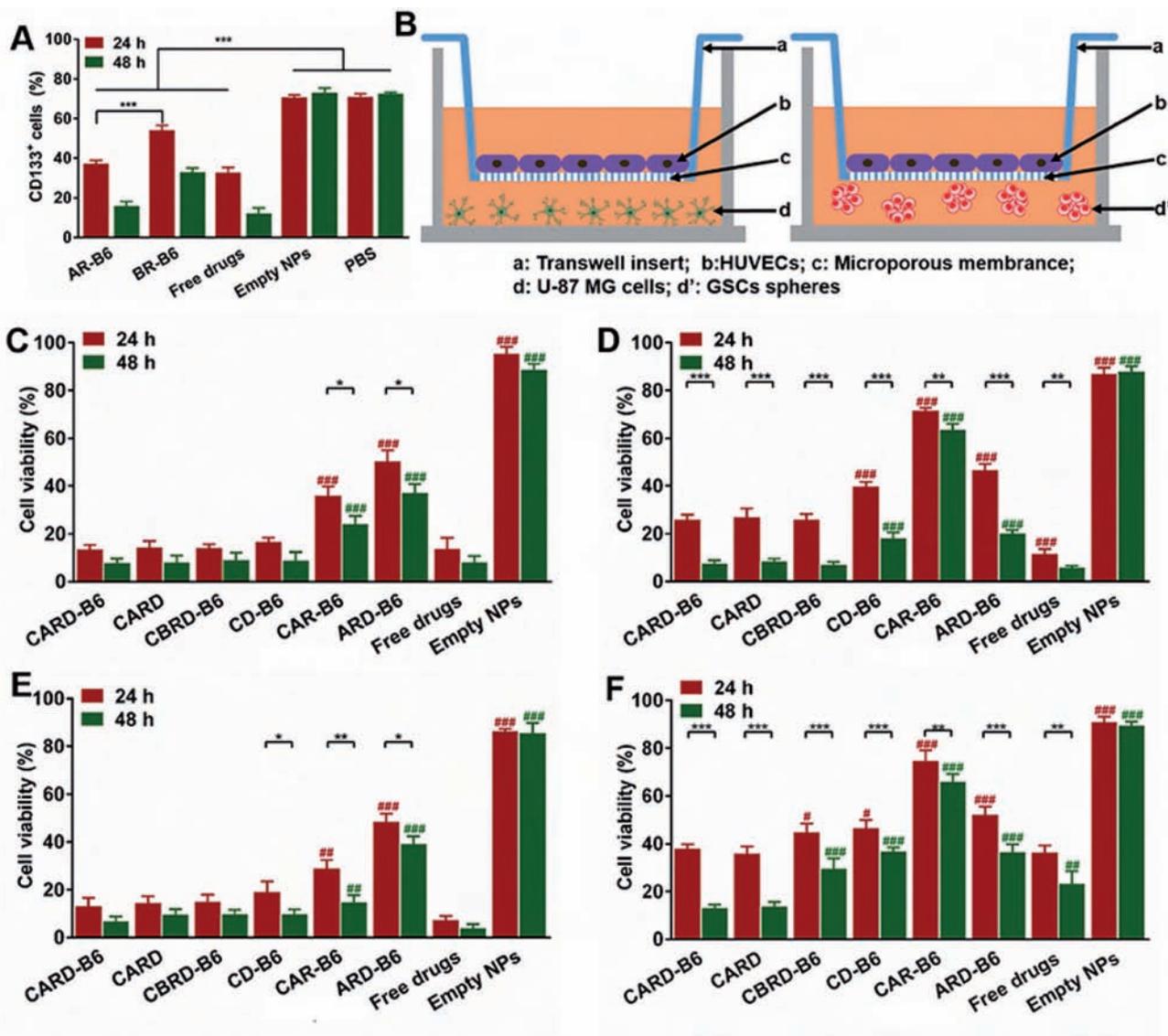FUNCTIONAL
MATERIALS**
www.afm-journal.de

Figure 5. Antitumor effect in vitro. A) The differentiation of GSCs induced by different samples was detected by flow cytometric analysis of CD133 expression. B) HUVECs/U-87 MG cells and HUVECs/GSCs spheres cocultured model were constructed to imitate tumor tissue. The cell viability of C) HUVECs, D) U-87 MG cells cocultured in HUVECs/U-87 MG cells model and E) HUVECs, F) GSCs spheres cocultured in HUVECs/GSCs spheres after 24 and 48 h treatment with different samples, respectively. The mean ± SD is shown ($n = 3$). *: differences between groups below the black line. *$P < 0.05$, **$P < 0.01$, ***$P < 0.005$. #: differences between other samples and CARD-B6 for 24 h. #$P < 0.05$, ##$P < 0.01$, ###$P < 0.005$. #: differences between other samples and CARD-B6 for 48 h. ##$P < 0.01$, ###$P < 0.005$.

for CARD-B6. The results indicated that CARD-B6 could significantly extend the circulation time of the drugs due to their excellent serum stability.

CARD-B6 could readily penetrate into glioblastoma cells in the in vitro BBB model due to the modification of B6. The permeability of CARD-B6 across the BBB in vivo was measured via MRI of the SPIONs in the traceable NPs. Intracranial glioblastoma-bearing mice were treated with CARD-B6 and CARD via intravenous injection. The T2* MRI was then performed after 12, 24, 36 and 48 h. As shown in Figure 6C, the accumulation of CARD-B6 in the tumor region was detected after 12 h and reached a maximum at 24 h. There was no MR signal at 48 h, which suggested that CARD-B6 were metabolized 48 h after the

injection. In comparison, only weak MR signal was detected for CARD at 24 h (Figure 6D). These results showed that CARD-B6 with a long circulation time was efficiently accumulated in the brain due to the recognition between B6 and the transferrin receptor expressed in the endothelial cells of the BBB.

To further evaluate the targeted ability of CARD-B6, the biodistribution of particles after intravenous injection was detected via a Kodak in vivo imaging system. As shown in Figure S20 (Supporting Information), CARD and free drugs (CA4+ATRA+DOX) could hardly penetrate the BBB and most of them accumulated in liver and kidney after 24 h injections. In comparison, most of CARD-B6 were accumulated in brain instead of other organs. These results indicated that
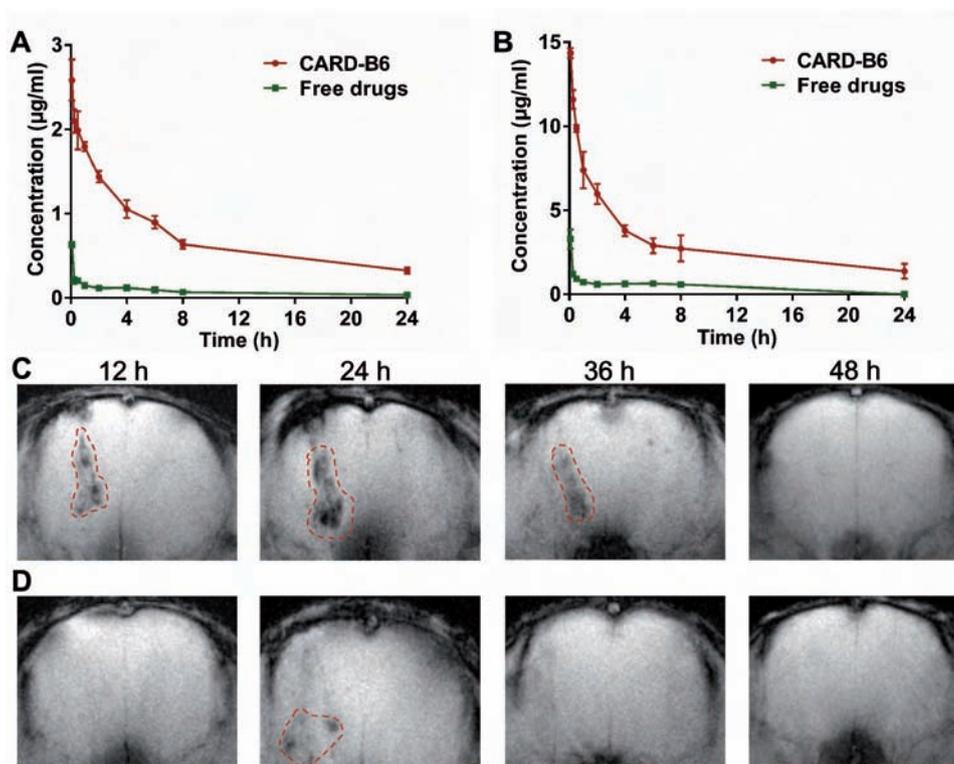
**ADVANCED
SCIENCE NEWS**
www.advancedsciencenews.com

**ADVANCED
FUNCTIONAL
MATERIALS**
www.afm-journal.de

Figure 6. Pharmacokinetics and accumulation of the traceable NPs in the tumor region. Plasma concentrations of A) CA4 and B) DOX in different samples at different time points. T2* MRI after treating intracranial glioblastoma-bearing mice at different time points with C) CARD-B6 and D) CARD via intravenous injection.

B6 modification could significantly improve the ability of CARD-B6 across BBB.

2.8. In Vivo Antitumor Studies

To further evaluate the in vivo antitumor effect of CARD-B6, intracranial U-87 MG tumor-bearing nude mice were treated with different formulations via intravenous injection of equivalent drug doses of 0.5 mg CA4/kg, 2.5 mg DOX/kg and 0.5 mg ATRA/kg. After inoculation for 16 d, drugs were injected every other day until the end of treatment. As shown in **Figure 7**A, the death of mice treated with PBS occurred 21 d after the inoculation. Specifically, at 30 d, 100% mice treated with CARD had died, whereas a 100% survival was achieved for mice treated with CARD-B6 at the same time point due to the high permeability of the BBB. At the completion of the treatment, there were 60% survival mice after treating with CARD-B6 and all other groups' mice were died. The results indicated that CARD-B6 with high permeability of the BBB and ability of spatiotemporally controlled release could enhance the antitumor effect of DOX on GBM with extended survival time.

Next, the effects of the NPs on angiogenesis, GSCs, and glioblastoma cells were analyzed. Blood flow was clearly visible in the laser speckle contrast analysis images (Figure 7B, and Videos S1–S5, Supporting Information). The excessive and grossly disorganized blood flow provided the voracious nutrients demands for rapid tumor growth. After treatment with PBS and other groups, the excessive disorganized blood

flow was still observed in the tumor region. In comparison, almost no blood flow existed in the tumor region following treatment with CARD-B6. The ratios of flux mean between the tumor regions and the contralateral normal regions were further quantified as shown in Figure 7C. The ratio of flux mean for the CARD-B6 group decreased to 0.74, which was significantly lower than the value for the CARD (1.03), ARD-B6 (1.24), free drugs (CA4 + ATRA + DOX) (1.23), and PBS group (1.76). This result further suggested that CARD-B6 could facilitate the delivery of CA4 into the tumor region and the first-released CA4 significantly destroyed the angiogenesis and cut off the nutrition supply for the rapid growth of the GBM. To further confirm their antivascular effect, the tumor vasculature was stained with an anti-CD31 antibody (Figure S21, Supporting Information).[25] Compared with the controls, CARD-B6 significantly reduced the tumor angiogenesis, which removed the protection of the glioblastoma cells and GSCs.

The differentiation of the GSCs after treatment was quantified by the CD133 antibody. As shown in Figure 7D, the CARD-B6 treatment resulted in a dramatic reduction of CD133+ GSCs in the residual tumor cells. In comparison, the effect of induction differentiation for the CARD, CBRD-B6, CD-B6, and free drugs treatment was not obvious. This result showed that the rapidly released ATRA induced the GSCs differentiation into glioblastoma cells and overcame their chemoresistance, which enhanced the therapeutic effect of DOX.

In order to outline the contribution of CARD-B6 to DOX for the GBM therapy, the density of apoptotic cells in the malignant tissue was further assessed by terminal
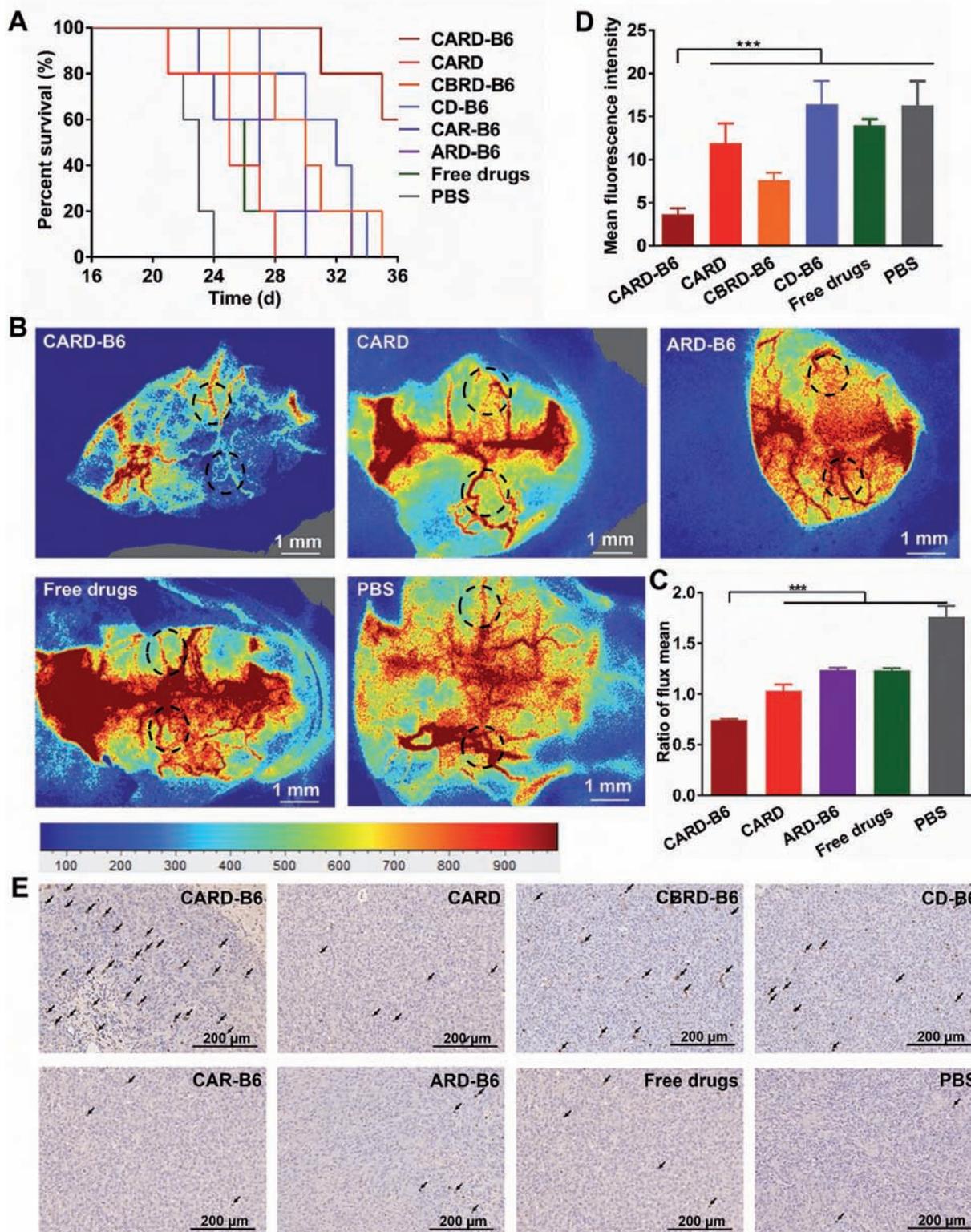
ADVANCED
SCIENCE NEWS
www.advancedsciencenews.com

ADVANCED
FUNCTIONAL
MATERIALS
www.afm-journal.de

Figure 7. Antitumor effect of the traceable NPs in vivo. Intracranial U-87 MG tumor-bearing nude mice were treated with different formulations via intravenous injection every other day for 16 d after inoculation. A) The survival curve of the mice in all groups. B) The laser speckle contrast analysis images of glioblastoma after treatment. The below circles represented tumor region and the upper circles represented contralateral normal region. The scale bars correspond to 1 mm. C) The quantitative results of image B. D) The GSCs ratio within tumor after tumor suppression study. E) TUNEL images of tumor regions after treatment. The scale bars correspond to 200 μm. The arrows represented apoptotic cells in TUNEL analysis. The mean ± SD is shown ($n = 3$). ***$P < 0.005$.

deoxynucleotidyltransferase mediated UTP end labeling (TUNEL) analyses. As shown in Figure 7E, CARD-B6 exhibited the best apoptosis of the tumor cells compared to the other groups. The damage of CARD-B6 to the healthy brain tissue was then assessed. As shown in Figure S22 (Supporting Information), there was no apoptotic cell in healthy brain tissue. These results indicated that CARD-B6 with spatiotemporally controlled release ability could maximize the effectiveness of DOX for the treatment of GBM by means of overcoming the problems associated with the BBB, tumor vasculature, and chemotherapy resistance of the GSCs, which further prolonged the survival time of intracranial U-87 MG tumor-bearing nude mice.

3. Conclusions

In this study, traceable codelivery system termed CARD-B6 were successfully developed. CARD-B6 delivered CA4, ATRA, and DOX to their corresponding active sites sequentially after crossing the BBB, which significantly enhanced the therapeutic efficacy of DOX on GBM. It showed that CARD-B6 with excellent serum stability significantly extended the circulation time of the drugs. The modification of B6 improved the ability of the NPs to permeate into the tumor mass, which was traced by cubic SPIONs for MRI. After accumulating in the tumor mass, the first-released CA4 via the protonation of PAE in an extracellular microenvironment of pH 6.5 destroyed the blood vessels to promote the interaction between the tumor mass and CARD-B6. In glioblastoma cells, DOX and ATRA were released simultaneously via the breakage of the amido bond to induce the apoptosis synergistically. In the GSCs, ATRA was rapidly released due to the quick breakage of the AZO bond under hypoxic environment, which induced the differentiation of GSCs and enhanced their sensitivity to the subsequently released DOX. With spatiotemporally ability, CARD-B6 was able to overcome the issues of using DOX for GBM therapy and significantly improved the cytotoxicity of DOX for the glioblastoma cells and the GSCs both in vitro and in vivo, holding great potential for GBM therapy.

Supporting Information

Supporting Information is available from the Wiley Online Library or from the authors.

Acknowledgements

Conflict of Interest

The authors declare no conflict of interest.

Keywords

[1] C. Carvalho, R. X. Santos, S. Cardoso, S. Correia, P. J. Oliveira, M. S. Santos, P. I. Moreira, *Curr. Med. Chem.* **2009**, *16*, 3267.

[2] a) S. Agarwal, R. Sane, R. Oberoi, J. R. Ohlfest, W. F. Elmquist, *Expert Rev. Mol. Med.* **2011**, *13*, e17; b) M. E. Hardee, D. Zagzag, *Am. J. Pathol.* **2012**, *181*, 1126; c) B. Auffinger, D. Spencer, P. Pytel, A. U. Ahmed, M. S. Lesniak, *Expert Rev. Neurother.* **2015**, *15*, 741.

[3] a) A. Singh, W. Kim, Y. Kim, K. Jeong, C. S. Kang, Y. Kim, J. Koh, S. D. Mahajan, P. N. Prasad, S. Kim, *Adv. Funct. Mater.* **2016**, *26*, 7057; b) T. Lammers, P. Koczera, S. Fokong, F. Gremse, J. Ehling, M. Vogt, A. Pich, G. Storm, M. van Zandvoort, F. Kiessling, *Adv. Funct. Mater.* **2015**, *25*, 36.

[4] a) R. J. Gilbertson, J. N. Rich, *Nat. Rev. Cancer* **2007**, *7*, 733; b) J. Jo, D. Schiff, B. Purow, *Expert Rev. Neurother.* **2012**, *12*, 733.

[5] a) C. Lu, A. Shervington, *Mol. Cell. Biochem.* **2008**, *312*, 71; b) C. Ciceroni, M. Bonelli, E. Mastrantoni, C. Niccolini, M. Laurenza, L. M. Larocca, R. Pallini, A. Traficante, P. Spinsanti, L. Ricci-Vitiani, A. Arcella, R. De Maria, F. Nicoletti, G. Battaglia, D. Melchiorri, *Cell Death Differ.* **2013**, *20*, 396.

[6] J. Park, M. Aryal, N. Vykhodtseva, Y. Z. Zhang, N. McDannold, *J. Controlled Release* **2017**, *250*, 77.

[7] S. Dhar, E. M. Reddy, A. Prabhune, V. Pokharkar, A. Shiras, B. L. V. Prasad, *Nanoscale* **2012**, *4*, 7878.

[8] a) G. C. Tron, T. Pirali, G. Sorba, F. Pagliai, S. Busacca, A. A. Genazzani, *J. Med. Chem.* **2006**, *49*, 3033; b) D. Huang, S. Zhang, T. Zhong, W. Ren, X. Yao, Y. Guo, X. C. Duan, Y. F. Yin, S. S. Zhang, X. Zhang, *Oncotarget* **2016**, *7*, 43616.

[9] a) M. Ying, S. Wang, Y. Sang, P. Sun, B. Lal, C. R. Goodwin, H. Guerrero-Cazares, A. Quinones-Hinojosa, J. Laterra, S. Xia, *Oncogene* **2011**, *30*, 3454; b) S. Karmakar, N. L. Banik, S. K. Ray, *Cancer* **2008**, *112*, 596.

[10] a) R. Zhang, N. L. Banik, S. K. Ray, *Neurochem. Res.* **2007**, *32*, 2194; b) A. Das, N. L. Banik, S. K. Ray, *J. Neuro-Oncol.* **2008**, *87*, 9.

[11] a) Z. Liu, X. Gao, T. Kang, M. Jiang, D. Miao, G. Gu, Q. Hu, Q. Song, L. Yao, Y. Tu, H. Chen, X. Jiang, J. Chen, *Bioconjugate Chem.* **2013**, *24*, 997; b) F. Zhang, C. L. Xu, C. M. Liu, *Drug Des., Dev. Ther.* **2015**, *9*, 2089.

[12] a) T. D. Sun, W. Cui, M. Yan, G. Qin, W. Guo, H. X. Gu, S. Q. Liu, Q. Wu, *Adv. Mater.* **2016**, *28*, 7397; b) Y. T. Gao, G. X. Feng, T. Jiang, C. C. Goh, L. G. Ng, B. Liu, B. Li, L. Yang, J. L. Hua, H. Tian, *Adv. Funct. Mater.* **2015**, *25*, 2857.

[13] X. P. Duan, J. S. Xiao, Q. Yin, Z. W. Zhang, H. J. Yu, S. R. Mao, Y. P. Li, *Acs Nano* **2013**, *7*, 5858.

[14] a) A. Mohyeldin, T. Garzon-Muvdi, A. Quinones-Hinojosa, *Cell Stem Cell* **2010**, *7*, 150; b) M. P. Mongiardi, *CNS Neurol. Disord.: Drug Targets* **2012**, *11*, 878.

[15] Y. Li, R. Zhang, Z. Lu, G. Ma, L. Chen, Q. Tang, X. Zhang, *Small* **2016**, *12*, 5516.

[16] a) H. Marie, L. Lemaire, F. Franconi, S. Lajnef, Y. M. Frapart, V. Nicolas, G. Frebourg, M. Trichet, C. Menager, S. Lesieur, *Adv. Funct. Mater.* **2015**, *25*, 1258; b) J. Huang, Y. C. Li, A. Orza, Q. Lu, P. Guo, L. Y. Wang, L. Yang, H. Mao, *Adv. Funct. Mater.* **2016**, *26*, 3818; c) N. Lee, Y. Choi, Y. Lee, M. Park, W. K. Moon, S. H. Choi, T. Hyeon, *Nano Lett.* **2012**, *12*, 3127.

[17] W. Lu, C. Y. Xiong, R. Zhang, L. F. Shi, M. Huang, G. D. Zhang, S. L. Song, Q. Huang, G. Y. Liu, C. Li, *J. Controlled Release* **2012**, *161*, 959.

[18] Y. G. Wang, K. J. Zhou, G. Huang, C. Hensley, X. N. Huang, X. P. Ma, T. Zhao, B. D. Sumer, R. J. DeBerardinis, J. M. Gao, *Nat. Mater.* **2014**, *13*, 204.

[19] Y. Cheng, R. Morshed, S. H. Cheng, A. Tobias, B. Auffinger, D. A. Wainwright, L. J. Zhang, C. Yunis, Y. Han, C. T. Chen, L. W. Lo, K. S. Aboody, A. U. Ahmed, M. S. Lesniak, *Small* **2013**, *9*, 4123.

[20] J. Li, X. K. Hu, R. H. Lipson, *Anal. Chem.* **2013**, *85*, 5499.

[21] S. Tang, Q. Yin, J. H. Su, H. P. Sun, Q. S. Meng, Y. Chen, L. L. Chen, Y. Z. Huang, W. W. Gu, M. H. Xu, H. J. Yu, Z. W. Zhang, Y. P. Li, *Biomaterials* **2015**, *48*, 1.

[22] R. Stangenberg, Y. Wu, J. Hedrich, D. Kurzbach, D. Wehner, G. Weidinger, S. L. Kuan, M. I. Jansen, F. Jelezko, H. J. Luhmann, D. Hinderberger, T. Weil, K. Mullen, *Adv. Healthcare Mater.* **2015**, *4*, 377.

[23] Y. Li, R. Y. Liu, J. Yang, Y. J. Shi, G. H. Ma, Z. Z. Zhang, X. Zhang, *Biomaterials* **2015**, *41*, 1.

[24] B. L. Hu, Q. H. Wang, Y. A. Wang, S. J. Hua, C. E. G. Sauve, D. Ong, Z. D. Lan, Q. Chang, Y. W. Ho, M. M. Monasterio, X. Lu, Y. Zhong, J. H. Zhang, P. N. Deng, Z. Tan, G. C. Wang, W. T. Liao, L. J. Corley, H. Y. Yan, J. X. Zhang, Y. P. You, N. Liu, L. B. Cai, G. Finocchiaro, J. J. Phillips, M. S. Berger, D. J. Spring, J. Hu, E. P. Sulman, G. N. Fuller, L. Chin, R. G. W. Verhaak, R. A. DePinho, *Cell* **2016**, *167*, 1281.

[25] T. A. Cheema, H. Wakimoto, P. E. Fecci, J. F. Ning, T. Kuroda, D. S. Jeyaretna, R. L. Martuza, S. D. Rabkin, *P. Natl. Acad. Sci. USA* **2013**, *110*, 12006.